Generation of chimeric respiratory viruses with altered tropism by coinfection of influenza A virus and respiratory syncytial virus

Authors: Joanne Haney[1], Swetha Vijayakrishnan[1], James Streetley[2], Kieran Dee[1], Daniel Max Goldfarb[1], Mairi Clarke[2], Margaret Mullin[3], Stephen D Carter[1], David Bhella[1,2] and Pablo R Murcia[1]

Affiliations:

[1]MRC-University of Glasgow Centre for Virus Research, Institute of Infection, Immunity and Inflammation, College of Medical, Veterinary and Life Sciences, University of Glasgow, Glasgow, Scotland, UK.

[2]Scottish Centre for Macromolecular Imaging, College of Medical, Veterinary and Life Sciences, University of Glasgow, Glasgow, Scotland, UK.

[3]Glasgow Imaging Facility, Institute of Infection, Immunity and Inflammation, College of Medical, Veterinary and Life Sciences, University of Glasgow, Glasgow, Scotland, UK.

Correspondence: Pablo.murcia@glasgow.ac.uk

Summary

Interactions between co-circulating respiratory viruses are recognized for their impact on viral transmission and clinical outcomes. However, the consequences of these virus-virus interactions at the cellular level are unclear. We coinfected human lung cells with influenza A virus (IAV) and respiratory syncytial virus (RSV). Super-resolution microscopy combined with live-cell imaging and scanning electron microscopy identified extracellular and membrane-associated filamentous structures, likely composed of elements of both IAV and RSV virions. Cryo-electron tomography confirmed the presence of chimeric virus particles exhibiting glycoproteins and ribonucleoproteins of both parental viruses. Functional assays revealed chimeric particles facilitate IAV infection in cells depleted of IAV receptors, demonstrating expanded tropism. Our observations define a previously unknown interaction that is likely to affect virus pathogenesis and have profound implications for infection biology.

Main Text

Viruses are intracellular pathogens whose replication success relies on the infection of a restricted subset of cell types, a property known as tropism. As multiple viruses exhibit the same tropism, cells and tissues are susceptible to infection by a community of taxonomically diverse viruses. From this perspective, a given tissue or body compartment can be considered an ecological niche in which members of a virus community co-exist. Coinfections by more than one virus represent between ~10-30% of all respiratory viral infections and are commonly observed among children (*1*, *2*). The clinical impact of viral coinfections is unclear: while some studies indicate that coinfections do not alter the outcome of disease (*3*-*5*), others report increased incidence of viral pneumonia (*6*, *7*). At the cellular level, the underlying viral interactions that determine the outcome of coinfections are unclear. Direct interactions between viruses within coinfected cells can result in substantial changes to the viral progeny. Outcomes of interactions can include pseudotyping (incorporation of surface proteins from a different virus) or genomic rearrangements, which may generate novel strains with pandemic potential such as SARS-CoV-2 and pandemic influenza A viruses (*11*, *12*).

Here we examine interactions between two commonly co-circulating viruses of high clinical importance: IAV and respiratory syncytial virus (RSV). IAV accounts for over five million hospitalizations each year (*13*) and the emergence of novel IAV pandemic strains represents a constant threat to global health. RSV is the leading cause of acute lower respiratory tract infection in children under five years of age, with 99% RSV-related mortality occurring in low- and middle-income countries (*14*, *15*). In the United Kingdom alone, RSV causes over 8,000 deaths annually (*16*). To better understand the molecular basis of virus-virus interactions we developed an integrated workflow that combines classical virology, super-resolution microscopy, live-cell imaging, scanning electron microcopy (SEM) and cryo-electron tomography (cryo-ET). We used this workflow to unveil previously unknown direct intracellular interactions between IAV and RSV. We envision this workflow will have broad applicability to study other virus-virus interactions between clinically important viruses.

To study virus-virus interactions during confection, we infected A549 cells, an interferon-competent cell line derived from human lung (*17*), with a mixed inoculum of IAV and RSV, or individual virus controls. Infections were carried out at high multiplicity of infection (MOI) to facilitate coinfection and recapitulate high MOIs produced in advanced stages of infection (when IAV and RSV infectious foci may come into contact). We compared viral

replication in single infection and coinfection. Single infection with IAV resulted in robust replication, peaking between 24-48 hours post infection (hpi). In coinfections, IAV replication was marginally, but consistently, increased in the presence of RSV (Fig. 1a, top left).

As RSV reached its peak of replication in single infection at a later timepoint than IAV (72 hpi, Fig. 1a, top right), further coinfections were performed to determine optimal conditions for coinfections by using a reduced IAV MOI (ten-fold reduction relative to RSV). The reduced IAV input did not negatively affect IAV replication and IAV still replicated to higher titres in coinfection compared to single infection (Fig. 1a, bottom left). In contrast, RSV titres were significantly reduced by over 400-fold at 72 hpi in the presence of IAV both at equivalent MOI (Fig. 1a, top right) and when IAV MOI was reduced relative to RSV (Fig. 1a, bottom right). Overall, these results show that RSV replication is reduced in the presence of IAV, whereas viral replication of the latter is unaffected in coinfection.

To assess if coinfection affected localization of viral proteins or viral cell-to-cell spread, single and coinfections were performed as described above and cells were fixed at 24 hpi. We performed immunofluorescence imaging using antibodies against the nucleoprotein (NP) of RSV and IAV. Cells infected with either RSV or IAV displayed features typical of each virus, such as cytoplasmic RSV NP inclusion bodies, or diffuse IAV NP staining within the nucleus and cytoplasm (Fig. 1b, left column). Similar features were observed in coinfected cells (Fig. 1b, boxed area) suggesting that co-infection did not affect the intracellular localization of viral proteins.

We quantified our immunofluorescence imaging data by counting the number of infected cells in single infections alongside the number of single infected and coinfected cells in coinfections. Figure 1c shows the proportion of cells infected with IAV or RSV, coinfected or uninfected at 24 hpi. Cell-to-cell spread of IAV or RSV was not negatively impacted by coinfection and most cells showed signs of coinfection at 24 hpi when infected with equivalent amounts of virus and when IAV input MOI was reduced 10-fold relative to RSV (Fig. 1c). This suggests that superinfection exclusion interactions do not prevent coinfection by IAV/RSV.

IAV and RSV are both enveloped viruses that target lipid rafts for assembly and budding at the plasma membrane (*18-20*). We therefore stained cells for the major glycoproteins of both viruses, IAV hemagglutinin (HA) and RSV fusion glycoprotein (F) (Fig. 1b, right column). In these experiments, IAV HA diffusely coated the plasma membrane of infected cells in

both single virus infection and coinfection. RSV F, however, was localized at discreet filamentous puncta extending from the cell surface, corresponding to budding RSV virions. Notably, in coinfected cells, HA was not excluded from RSV budding sites (Fig. 1b, right column, boxed area). We hypothesised that mixing of glycoproteins within these regions may result in incorporation of both IAV and RSV components to budding viral particles. To test this, we applied super-resolution confocal microscopy to image virions immunolabelled for HA and F at high resolution.

Confirming our hypothesis, super-resolution microscopy revealed dual-positive fluorescence suggesting the presence of budding viral filaments that have incorporated both IAV and RSV glycoproteins during coinfection (Fig. 2a, b). Strikingly, minimal colocalization between the two glycoproteins was observed; instead, glycoproteins were incorporated in distinct regions along the length of the filament, with most dual-positive filaments positive for IAV HA at the distal end (Extended Data Fig. 1). Furthermore, greater than half of coinfected cells (56±9.1%, mean ± SD) displayed dual-positive filaments that were cell associated. Many of these cells showed extensive production of dual-positive filaments, with no obvious indication of cell damage observed by nuclear or cellular morphology (Fig. 2c, d). We also observed filaments distant from coinfected cells that displayed similar dual-positive morphology, suggesting they had been remained intact upon release from coinfected cells (Fig. 2b). Nested among dual-positive filaments (both cell associated and released), we also identified filaments corresponding to IAV and RSV virions (identified by HA or F only staining) (Fig. 2a, b, Extended Data Fig. 1). This indicates that regions in which dual-positive filaments form may contain both IAV and RSV budding sites.

We then carried out live-cell microscopy to visualize the native organization of these filaments budding from coinfected cells. Consistent with our previous observations, we detected bundles of filaments protruding from the cell surface that incorporated F along the length of the filament with HA localized at the distal end (Fig. 2e).

Next, to achieve a greater understanding of the architecture of these budding viruses, scanning electron microscopy (SEM) was performed. IAV single infection revealed a pleomorphic population of membrane-associated structures consistent with spherical, bacilliform and filamentous particles, whereas RSV single infection resulted in dense clusters of budding RSV filaments (Extended Data Fig. 2). Interestingly, in coinfected cells we identified RSV–like filaments with structures branching from the distal ends resembling smaller bacilliform IAV-like virions (Fig. 2f). Taken together, our super-resolution

microscopy, live-cell imaging and SEM analysis suggest that coinfected cells likely produce filaments that possess elements of both IAV and RSV.

To determine the precise structural details of budding IAV/RSV filamentous viruses during coinfection we performed cryo-electron tomography (Cryo-ET). Cryo-ET enables the observation of viral particles in a native state, in three-dimensions and at macromolecular resolution. We identified structures consistent with pleomorphic IAV particles, as well as RSV filaments (Extended data file 1, Extended Data Movies 1-2). Importantly, we identified structures consistent with chimeric virus particles (CVPs) which contained elements of both IAV and RSV in 16 cryo-tomograms recorded. Unexpectedly, we consistently observed two classes of CVPs. In 4 cryo-tomograms we observed true chimeric viruses (CV, ~9% of the population), and in 12 cryo-tomograms we observed pseudotyped viruses (PV, ~27% of the population).

True chimeric viruses exhibited two distinct structural regions: the wider part of the filament was analogous in structure to RSV, which extended by a continuous membrane to a narrower region equivalent in structure to IAV at the distal end. (Fig. 3a-c, Extended data Fig. 3, Movies 1 and 2). Density consistent with both IAV and RSV RNP structure could be visualized and appear to be confined within their respective structural regions of the filaments (*21, 22*) (Fig. 3c-e). In addition, spikes consistent in size, shape and density with IAV or RSV glycoproteins could be identified coating the respective IAV or RSV-like regions of the CV (Fig. 3a). In some particles, the join between IAV and RSV regions had a clear lumen (Fig. 3a, b, Extended Data Fig. 3, Movie 1), whilst other CVs exhibited a much narrower join, with pinching of membranes between IAV and RSV regions (Fig. 3c, Extended Data Fig. 3, Movie 2). Furthermore, we noticed either single (Fig. 3a) or multiple IAV viruses (Fig. 3c) extending from the RSV viruses.

We also identified filaments consistent in structure with RSV virions that clearly contained RSV RNPs, yet had glycoprotein ordering that was markedly different to spikes commonly observed on RSV virions. These spikes closely resembled those on IAV virions and were most often observed at the distal end of filaments (*21, 22*). Consequently, we designated these structures "pseudotyped viruses" (Fig. 4f, g, Extended Data Fig. 4, Movie 3). To confirm this observation, statistical analysis was carried out to determine the inter-spike distance on IAV, RSV and PV filaments. Spike distances were measured from 11 control tomograms each for RSV and IAV, while spike-distance measurements were calculated from 4 tomograms for PV filaments (Fig. S4). RSV exhibited a mean (+/- SD) inter-spike spacing of 12.9 (+/-2.32) nm, while IAV had a spacing of 8.71 (+/-1.18) nm. Interestingly, PV

filaments had an average spike distance ranging from 8.31-9.56 nm, similar to IAV but significantly different to RSV ($p<0.0001$ by unpaired t-test) (Extended Data Fig. 4). Overall, our results unambiguously confirm the formation of chimeric forms of filaments (CV and PV) upon co-infection, which are structurally distinct from either parental virus.

As CVPs incorporate both IAV and RSV envelope glycoproteins, they could possess expanded tropism allowing them to infect cells that would otherwise be refractory to infection by one of the parental viruses. To test this hypothesis, we removed sialic acids (the receptor for IAV) from A549 cells by treating them with exogenous neuraminidase (NA) (Fig. 4a). Sialic acid removal was confirmed by staining cells with lectins that preferentially bind 2,3- sialic acids (Maackia Amurensis Lectin II [MAL II]) and terminal galactose residues that become exposed after sialic acid cleavage by NA (Erythrina Cristagalli Lectin [ECL]) (Fig. 4b). Single and coinfections were then performed, and the supernatant (containing released virus) and cell-associated virus fractions were collected. These fractions were subsequently used to inoculate IAV-receptor-deficient cells (NA-treated) or control cells (Fig. 4a). IAV entry in NA-treated cells was successfully blocked when inoculated with the supernatant of single IAV- infected cells, whereas entry of cell-associated IAV collected from single IAV infections was reduced by 85%. When NA-treated cells were inoculated with the supernatant or cell-associated fraction of mixed infections, IAV entry was significantly increased compared to IAV-only infection (Fig. 4c). The increase in IAV entry was more marked in the cell associated fraction and IAV entry in receptor-deficient cells was restored to 77% of the level of control cells. This was consistent with our imaging data showing a predominance towards cell associated CVPs. As RSV does not use sialic acids as receptors, no differences in RSV entry between NA-treated or control cells were detected (Fig. 4d). To determine if aggregation of viral particles may have contributed to IAV entry in NA-treated cells, we pre-incubated IAV and RSV to allow mixing and association of viral particles, before infecting NA-treated or control cells. No significant differences were observed in IAV or RSV entry into receptor-deficient cells compared to control cells when the viruses had been pre-mixed (Fig. 4d), compared to each virus alone. This indicates that IAV and RSV do not readily aggregate upon extracellular mixing, however virion aggregation may be influenced by more complex physiological factors *in vivo* (*23*). Overall, these findings indicate that IAV/RSV CVPs represent a subpopulation of infectious virus particles with expanded tropism, facilitating IAV entry by an alternative mechanism mediated by the RSV glycoproteins.

Discussion

Respiratory viruses are a group of taxonomically diverse pathogens that share a common tropism for the human respiratory tract and cause significant disease burden. While there is increasing evidence that interactions amongst viruses play an important role on virus dynamics and transmission, most of what is known about virus biology and pathogenesis is based on a tractable but reductionist research approach whereby each virus is studied in isolation.

Recent work provided evidence that interactions among respiratory viruses occur and have measurable outcomes at multiple levels, from populations, to individuals and tissues (*24-27*). However, studies characterizing direct virus-virus interactions within cells are scarce. Here we describe previously unknown interactions between IAV and RSV, two clinically important respiratory viruses that belong to different taxonomical families.

We show that in coinfections IAV replicates to higher titres, whereas RSV replication is reduced. The increase in IAV replication in the presence of RSV contrasts with the inhibition of IAV replication in coinfections with rhinovirus (*26*). This indicates that the consequences of coinfections are highly dependent on the viruses involved as they trigger virus-specific cellular responses.

We also show compelling evidence that coinfections can generate infectious chimeric virus particles composed of structural and genomic components of both parental viruses. The observation that CVPs can infect cells lacking IAV receptors suggests that coinfections can generate viruses with expanded tropism. This property may facilitate within host dissemination to areas within the respiratory tract that are refractory to infection by one of the parental viruses, which is likely to have a significant impact on pathogenesis and disease outcome. For example, IAV predominantly infects the upper and middle respiratory tract causing uncomplicated influenza, while RSV spreads more readily to the middle and lower respiratory tract (LRT) (*28-30*). Chimeric IAV/RSV viruses could play a *Trojan horse* role, that would enable IAV to spread to the LRT with subsequent potential complications, including viral pneumonia (*31*). In addition, as IAVs exhibit high mutation rates, LRT infections by CVPs might favor the selection of IAVs with increased tropism for the LRT and therefore result in selection of more pathogenic viruses. In recent years, a novel conceptual framework that incorporates social evolution theory has been developed to explain how virus-virus interactions can play an important role on virus function and fitness (*32*). Facilitation of viral spread by formation of CVPs aligns with the concept that, like other pathogens and organisms, viruses can engage in social-like traits that alter fitness and function.

Our results show that the generation of CVPs by coinfection is biologically feasible. The fact that IAV and RSV cocirculate in winter in the same populations (*1*), have a shared tropism for ciliated epithelial cells (*28, 33-35*) and bud from the apical cellular surface (*22, 33, 36*) suggest that CVPs have potential to be generated *in vivo*. The likelihood of a cell becoming coinfected during natural infection remains unknown, but will vary depending on the timing of infection and the localization of infectious foci within the respiratory tract. Estimates of viral bursts show that as viral load increases, the effective MOI to susceptible cells surrounding an infectious focus rapidly increases (*37*), enhancing the probability of cellular coinfection and therefore the potential generation of CVPs.

The formation of CVPs raises questions about basic and fundamental rules that govern viral assembly and budding. These processes, which are thought to be highly regulated, involve selective recruitment, trafficking (*38, 39*) and multimerization of viral proteins (*18, 40-42*) within specific compartments of the cell. While here we describe the formation of CVPs as a consequence of coinfection by IAV and RSV, we hypothesize that coinfections involving other pleomorphic enveloped viruses are also likely to generate CVPs. However, we pose that formation of infectious CVPs requires more than structural compatibility, and includes similar tropism, absence of superinfection exclusion or interference, as well as seasonal and geographical co-circulation. RSV is a pleomorphic enveloped virus with a broad tropism for different regions of the respiratory tract and is frequently observed in co-infections in winter (*43-45*) , therefore it is a good candidate to form CVPs with other respiratory viruses. This might explain some of the mechanisms that lead to viral pneumonia (*46*). Further studies will be required to address which virus combinations can generate infectious CVPs, which viral properties favor their formation, and more importantly, how they impact on pathogenesis and virus transmission.

Data Availability

Representative tomograms of the chimeric virus particles described in this paper have been deposited in the Electron Microscopy Data Bank (www.ebi.ac.uk/emdb) under accession codes EMD-13228 and EMD-13229.

References

1. S. Nickbakhsh et al., Extensive multiplex PCR diagnostics reveal new insights into the epidemiology of viral respiratory infections. Epidemiol Infect 144, 2064-2076 (2016).

2. A. Franz et al., Correlation of viral load of respiratory pathogens and co-infections with disease severity in children hospitalized for lower respiratory tract infection. J Clin Virol 48, 239-245 (2010).

3. E. A. Goka, P. J. Vallely, K. J. Mutton, P. E. Klapper, Single and multiple respiratory virus infections and severity of respiratory disease: a systematic review. Paediatr Respir Rev 15, 363-370 (2014).

4. M. C. Scotta et al., Respiratory viral coinfection and disease severity in children: A systematic review and meta-analysis. J Clin Virol 80, 45-56 (2016).

5. S. A. Asner et al., Clinical disease severity of respiratory viral co-infection versus single viral infection: a systematic review and meta-analysis. PLoS One 9, e99392 (2014).

6. S. A. Asner, W. Rose, A. Petrich, S. Richardson, D. J. Tran, Is virus coinfection a predictor of severity in children with viral respiratory infections? Clin Microbiol Infect 21, 264 e261-266 (2015).

7. I. A. Echenique et al., Clinical characteristics and outcomes in hospitalized patients with respiratory viral co-infection during the 2009 H1N1 influenza pandemic. PLoS One 8, e60845 (2013).

8. J. Zavada, The pseudotypic paradox. J Gen Virol 63 (Pt 1), 15-24 (1982).

9. A. Duverge, M. Negroni, Pseudotyping Lentiviral Vectors: When the Clothes Make the Virus. Viruses 12, (2020).

10. R. K. Akkina et al., High-efficiency gene transfer into CD34+ cells with a human immunodeficiency virus type 1-based retroviral vector pseudotyped with vesicular stomatitis virus envelope glycoprotein G. J Virol 70, 2581-2585 (1996).

11. G. J. Smith et al., Origins and evolutionary genomics of the 2009 swine-origin H1N1 influenza A epidemic. Nature 459, 1122-1125 (2009).

12. M. F. Boni et al., Evolutionary origins of the SARS-CoV-2 sarbecovirus lineage responsible for the COVID-19 pandemic. Nat Microbiol 5, 1408-1417 (2020).

13. K. E. Lafond et al., Global burden of influenza-associated lower respiratory tract infections and hospitalizations among adults: A systematic review and meta-analysis. PLoS Med 18, e1003550 (2021).

14. H. Nair et al., Global burden of acute lower respiratory infections due to respiratory syncytial virus in young children: a systematic review and meta-analysis. The Lancet 375, 1545-1555 (2010).

15. T. Shi et al., Global, regional, and national disease burden estimates of acute lower respiratory infections due to respiratory syncytial virus in young children in 2015: a systematic review and modelling study. The Lancet 390, 946-958 (2017).

16. D. M. Fleming et al., Modelling estimates of the burden of Respiratory Syncytial virus infection in adults and the elderly in the United Kingdom. BMC Infect Dis 15, 443 (2015).

17. G. R. Gaajetaan et al., Interferon-beta induces a long-lasting antiviral state in human respiratory epithelial cells. J Infect 66, 163-169 (2013).

18. J. S. Rossman, R. A. Lamb, Influenza virus assembly and budding. Virology 411, 229-236 (2011).

19. B. J. Chen, G. P. Leser, E. Morita, R. A. Lamb, Influenza virus hemagglutinin and neuraminidase, but not the matrix protein, are required for assembly and budding of plasmid-derived virus-like particles. J Virol 81, 7111-7123 (2007).

20. L. H. McCurdy, B. S. Graham, Role of plasma membrane lipid microdomains in respiratory syncytial virus filament formation. J Virol 77, 1747-1756 (2003).

21. S. Vijayakrishnan et al., Cryotomography of budding influenza A virus reveals filaments with diverse morphologies that mostly do not bear a genome at their distal end. PLoS Pathog 9, e1003413 (2013).

22. Z. Ke et al., The Morphology and Assembly of Respiratory Syncytial Virus Revealed by Cryo-Electron Tomography. Viruses 10, (2018).

23. J. M. Cuevas, M. Duran-Moreno, R. Sanjuan, Multi-virion infectious units arise from free viral particles in an enveloped virus. Nat Microbiol 2, 17078 (2017).

24. K. Dee et al., Human rhinovirus infection blocks SARS-CoV-2 replication within the respiratory epithelium: implications for COVID-19 epidemiology. J Infect Dis, (2021).

25. S. Nickbakhsh et al., Virus-virus interactions impact the population dynamics of influenza and the common cold. Proc Natl Acad Sci U S A, (2019).

26. A. Wu, V. T. Mihaylova, M. L. Landry, E. F. Foxman, Interference between rhinovirus and influenza A virus: a clinical data analysis and experimental infection study. Lancet Microbe 1, e254-e262 (2020).

27. N. R. Cheemarla et al., Dynamic innate immune response determines susceptibility to SARS-CoV-2 infection and early replication kinetics. J Exp Med 218, (2021).

28. J. E. Johnson, R. A. Gonzales, S. J. Olson, P. F. Wright, B. S. Graham, The histopathology of fatal untreated human respiratory syncytial virus infection. Mod Pathol 20, 108-119 (2007).

29. C. RM, K. HW, V. AJ, J. KM, P. RH, Respiratory syncytial virus. I. Virus recovery and other observations during 1960 outbreak of bronchiolitis, pneumonia, and minor respiratory diseases in children. Jama 176, 647-653 (1961).

30. S. Othumpangat, L. F. Gibson, L. Samsell, G. Piedimonte, NGF is an essential survival factor for bronchial epithelial cells during respiratory syncytial virus infection. PLoS One 4, e6444 (2009).

31. T. Kuiken, J. K. Taubenberger, Pathology of human influenza revisited. Vaccine 26 Suppl 4, D59-66 (2008).

32. S. L. Diaz-Munoz, R. Sanjuan, S. West, Sociovirology: Conflict, Cooperation, and Communication among Viruses. Cell Host Microbe 22, 437-441 (2017).

33. L. Zhang, M. E. Peeples, R. C. Boucher, P. L. Collins, R. J. Pickles, Respiratory syncytial virus infection of human airway epithelial cells is polarized, specific to ciliated cells, and without obvious cytopathology. J Virol 76, 5654-5666 (2002).

34. K. P. Hui et al., Tropism, replication competence, and innate immune responses of influenza virus: an analysis of human airway organoids and ex-vivo bronchus cultures. The Lancet Respiratory Medicine 6, 846-854 (2018).

35. N. H. Wu et al., The differentiated airway epithelium infected by influenza viruses maintains the barrier function despite a dramatic loss of ciliated cells. Sci Rep 6, 39668 (2016).

36. L. Kolesnikova et al., Influenza virus budding from the tips of cellular microvilli in differentiated human airway epithelial cells. J Gen Virol 94, 971-976 (2013).

37. L. Mohler, D. Flockerzi, H. Sann, U. Reichl, Mathematical model of influenza A virus production in large-scale microcarrier culture. Biotechnol Bioeng 90, 46-58 (2005).

38. E. A. Bruce, P. Digard, A. D. Stuart, The Rab11 pathway is required for influenza A virus budding and filament formation. J Virol 84, 5848-5859 (2010).

39. T. J. Utley et al., Respiratory syncytial virus uses a Vps4-independent budding mechanism controlled by Rab11-FIP2. Proc Natl Acad Sci U S A 105, 10209-10214 (2008).

40. D. S. Lyles, Assembly and budding of negative-strand RNA viruses. Adv Virus Res 85, 57-90 (2013).

41. P. Chlanda et al., Structural Analysis of the Roles of Influenza A Virus Membrane-Associated Proteins in Assembly and Morphology. J Virol 89, 8957-8966 (2015).

42. G. Kiss et al., Structural analysis of respiratory syncytial virus reveals the position of M2-1 between the matrix protein and the ribonucleoprotein complex. J Virol 88, 7602-7617 (2014).

43. Y. Li, P. Pillai, F. Miyake, H. Nair, The role of viral co-infections in the severity of acute respiratory infections among children infected with respiratory syncytial virus (RSV): A systematic review and meta-analysis. J Glob Health 10, 010426 (2020).

44. C. Calvo et al., Respiratory Syncytial Virus Coinfections With Rhinovirus and Human Bocavirus in Hospitalized Children. Medicine (Baltimore) 94, e1788 (2015).

45. L. M. Yoshida et al., Respiratory syncytial virus: co-infection and paediatric lower respiratory tract infections. Eur Respir J 42, 461-469 (2013).

46. O. Ruuskanen, E. Lahti, L. C. Jennings, D. R. Murdoch, Viral pneumonia. Lancet 377, 1264-1275 (2011).

Author contributions.

Author contributions are based on the CRediT taxonomy (https://casrai.org/credit/). J.H.: Investigation, Methodology, Formal analysis, Visualisation, Writing - original draft; S.V.: Investigation, Data curation, Formal analysis, Resources, Metodology, Validation, Visualisation, Supervision Writing- original draft; J.S.: Investigation, Writing – review and editing; K.D.: Investigation, Writing – review and editing; D.M.G.: Investigation, Writing – review and editing; M.C.: Investigation, Writing – review and editing; M.M.: Investigation, Methodology, Writing – review and editing; S.D.C: Formal analysis, writing, review and editing; D.B.: Resources, Funding acquisition, Writing – review and editing; P.R.M.: Conceptualization, Methodology, Validation, Data curation, Supervision, Funding acquisition, Project administration, Writing – original draft.

Acknowledgments

This work was supported by grants from the Medical Research Council of the United Kingdom (MC_UU_12014/9 to PRM, MR/N013166/1 to JH, MR/R502327/1 to DMG, MC_UU_12014/7 to SV, and MC_UU_12014/7 to DB). The Scottish Centre for Macromolecular Imaging (SCMI) is funded by the MRC (MC_PC_17135) and SFC (H17007).

Conflicts of interest. The authors declare no conflicts of interest.

Correspondence and requests for materials should be addressed to Pablo Murcia.

Reprints and permissions information is available at www.nature.com/reprints.

Figures

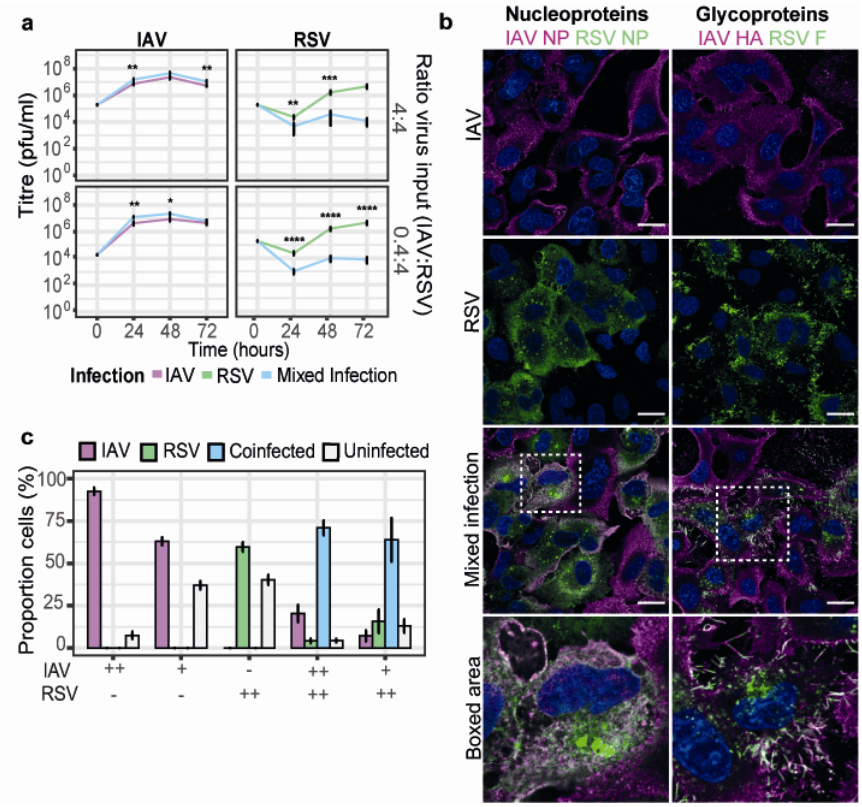

Figure 1. Replication kinetics and cell to cell spread are affected in IAV and RSV coinfections. (**A**) Left panel, IAV replication kinetics in single infection (magenta line) and mixed infection with RSV (blue line). Right panel, RSV replication kinetics in single infection (green line) and mixed infection with IAV (blue line). Top row, infections carried out at equivalent MOI (4:4), bottom row, IAV input 10-fold less than RSV input (0.4:4). Error bars represent standard error, significance determined by Mann-Whitney test, * $p<0.05$, ** $p<0.01$, *** $p<0.001$, **** $p<0.0001$. (**B**) Immunofluorescence staining showing IAV nucleoprotein (magenta) and RSV nucleoprotein (green) in single infection and mixed infection (left column) and IAV haemagglutinin (magenta) and RSV fusion glycoprotein (green) in single and mixed infection (right column). Nuclei are stained with DAPI (blue). White boxes indicate regions in labelled boxed area, scale bar indicates 20 µm. (**C**) Percentage of cells infected with IAV-only (magenta), RSV-only (green), coinfected (blue) or uninfected (grey) in single virus infection or mixed at 24 hpi. Panel below plot represents the infection conditions used: - for no virus, ++ for MOI 4 and + for MOI 0.4.

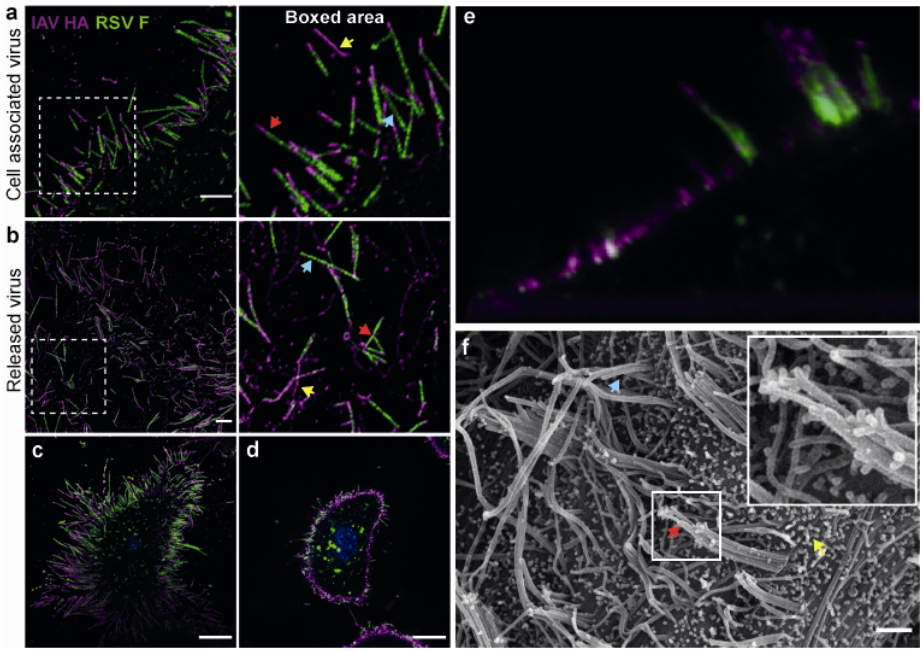

Figure 2. Coinfected cells display budding viral particles incorporate elements of both IAV and RSV. Cell associated viral filaments positive for IAV HA (magenta on merged image) and RSV F (green on merged image) that are cell associated (**A**) or released (**B**) from coinfected cells, imaged by super-resolution microscopy. Magnified images of white boxed regions indicate examples of IAV filaments (yellow arrows), RSV filaments (blue arrows) and dual-positive filaments (red arrows). Scale bars indicate 500 nm. (**C** and **D**) Coinfected cell exhibiting extensive dual-positive filament formation. Cell imaged by confocal microscopy at two Z-positions: basal side adhered to coverslip (**C**) and through the centre of the cell (**D**). Scale bars indicate 10 µm. (**E**) 2D z-plane image reconstructed from a Z-stack of a live cell stained for IAV HA and RSV F, imaged by super-resolution confocal microscopy at 100 nm intervals through the entire cell (16.3 µm). (F) Scanning electron micrograph of coinfected cell surface. IAV and RSV particles are indicated by yellow and blue arrows respectively. Red arrow and magnified region highlight particles that contain structural features of both IAV and RSV. Scale bar indicates 1 µm.

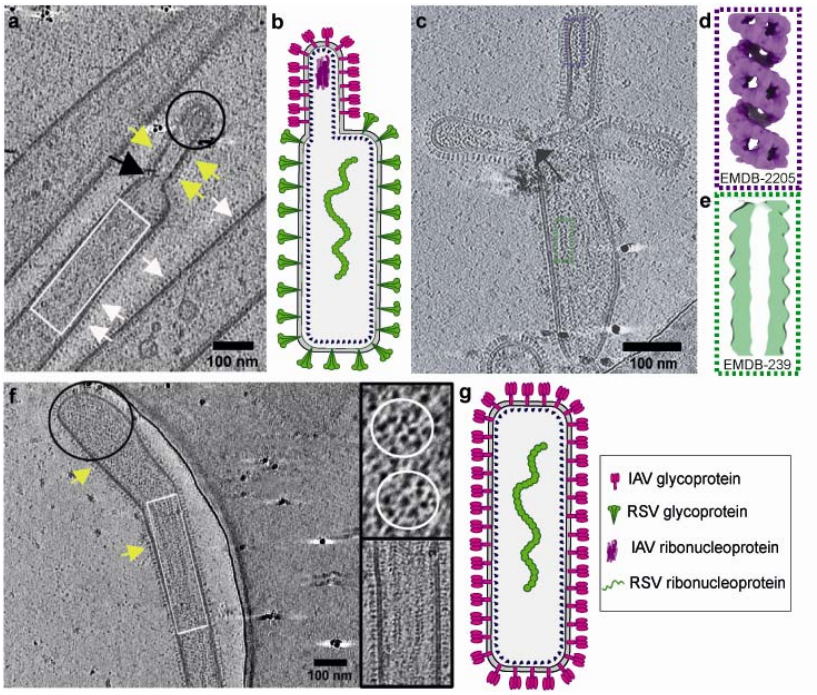

Figure 3. Cryo-ET reveals formation of chimeric virus particles containing structural components of both IAV and RSV virions. (**A**) True chimeric virus particle (CV) comprised of RSV- and IAV-like structural regions with a wide membrane join and a clear lumen (indicated by black arrow) between the structural components. RSV RNPs and glycoproteins (indicated by white box and arrows respectively) were contained to the RSV-like structural region, while IAV RNPs and glycoproteins (indicated by black circle and yellow arrows respectively) were contained to the IAV-like structural region at the distal end of the filament. (**B**) Schematic depicting CV structure and incorporation of IAV and RSV components. (**C**) Other CVs comprised of RSV with multiple IAV virions fused by narrow membrane joins (indicated by black arrow). Magenta boxed region highlights IAV RNPs, consistent in structure with published IAV RNP helical structure (EMDB-2205) shown in (**D**) in magenta dashed box. Green boxed region highlights RSV RNPs consistent in structure with (**E**) published RSV RNP structure (EMDB-2391), cross section shown in large green dashed box. (**F**) Pseudotyped particles (PV) comprised of filaments with RSV RNPs (indicated by white rectangle and the magnified view of the same region black box), decorated largely with IAV glycoproteins along the viral membrane (yellow arrows, black circle and magnified view in black box; magnified view of the top surface of the filament showing spikes exhibiting an IAV-like organisation). (**G**) Schematic depicting PV structure.

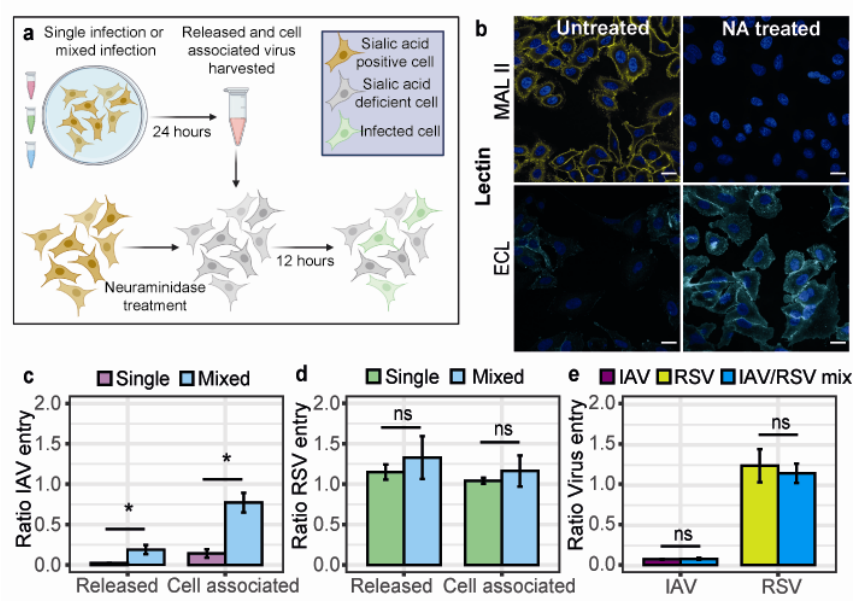

Figure 4. Virus produced from coinfection facilitates IAV infection in sialic acid-depleted cells. (**A**) Schematic representation of the experimental design involving inoculation of NA-treated sialic acid deficient cells with virus produced from single infection or coinfection. Figure created with Biorender. (**B**) NA-treated and untreated cells stained with Maackia Amurensis Lectin II (MAL II) in yellow (top row) and Erythrina Cristagalli Lectin (ECL) in cyan (bottom row). (**C**) Ratio of IAV entry into NA-treated cells versus control cells when harvested from single infection (magenta bars) or mixed infection (blue bars). (**D**) Ratio of RSV entry into NA-treated cells over control cells when harvested from single infection (green bars) or mixed infection (blue bars). (**E**) Ratio of virus entry of IAV only (magenta bar) or RSV only (green bar) into NA-treated over control cells, compared to entry of IAV pre-mixed with RSV or RSV pre-mixed with IAV into NA-treated over control cells (blue bars). Error bars represent standard error and significance was determined by Welch's t-test with, ns $p>0.05$, * $p<0.05$.

Movie 1: Video showing serial sections through the z-axis of a tomogram of a CVP with a single IAV region, formed during coinfection of IAV and RSV (corresponding image shown in Figure 4A). Glycoproteins and RNPs of both IAV and RSV are labeled and denoted by arrows.

Movie 2: Video showing serial sections through the z-axis of a tomogram of a CV with multiple IAV components, formed during coinfection of IAV and RSV (corresponding image

shown in Figure 4C). Glycoproteins and RNPs of both IAV and RSV are labeled and denoted by arrows.

Movie 3: Video showing serial sections through a tomogram of a pseudotype chimeric viral filament generated during IAV and RSV coinfection (corresponding image shown in Figure 4D). Glycoproteins and RNPs are labeled and denoted by arrows.

Reagents & Methods

Reagents

Cells

Human lung adenocarcinoma cells (A549) (American Type Culture Collection [ATCC], CCL-185), Madin Darby canine kidney (MDCK) cells (ATCC, CCL-34) and hEP-2 (ATCC, CCL-23) cells were cultured in Dulbecco's Minimum Essential Media (DMEM), high glucose, GlutaMAX supplemented with 10% fetal bovine serum (FBS).

Viruses

H1N1 influenza A/Puerto Rico/8/34 was rescued as previously described (47) and virus stocks were grown in MDCK cells. RSV strain A2 (American Type Culture Collection, VR-1540) was grown in hEP-2 cells.

Antibodies

The following primary antibodies were used at optimised concentrations: RSV fusion glycoprotein (Abcam, UK, AB24011, 1/1000), RSV nucleoprotein (Abcam, UK, AB22501, 1/1500), antisera to influenza A H1 (A/Puerto Rico/8/34, 1/1000) (NIBSC, UK, 03/242), influenza A virus nucleoprotein (European Veterinary Society, EVS238, 1/1000). Secondary antibodies: Rabbit anti-mouse IgG alexafluor 488 conjugate (Sigma-Aldrich, USA, SAB4600056, 1/1000), donkey anti-mouse 594 conjugate (Abcam, UK, ab150108, 1/1000) donkey anti-sheep alexafluor 594 conjugate (Thermo Fisher Scientific, USA, A-11016, 1/1000).

Methods

Virus growth curves

A549 cells were infected with IAV, RSV or synchronously infected with a mixed inoculum of IAV and RSV, diluted in DMEM, with 2% FBS and 1µg/ml trypsin TPCK. Infections were carried out with RSV at a multiplicity of infection (MOI) of 4 and IAV at an MOI of 4 or 0.4. A549 cells were inoculated in 48-well plates and incubated at 37˚C, 5% CO2 for 90 minutes, before the inoculum was removed and replaced with DMEM, with 2% FBS and 1µg/ml trypsin TPCK. Cells were incubated at 37˚C, 5% CO2 and supernatant from each infection was collected at 24, 48 and 72 hours post infection and stored at -80˚C prior to titration by plaque assay. Infectious titre was determined by plaque assay in MDCK cells or hEP-2 cells for IAV and RSV, respectively. Validation was carried out prior to these experiments to ensure specific detection of IAV or RSV plaques in the respective cell type. Viruses were titrated in 10-fold serial dilutions in duplicate and incubated on confluent cell monolayers for 90 minutes. For IAV plaque assays, overlay containing DMEM, 1µg/ml trypsin TPCK and 0.6% Avicel was used and plates were incubated at 37˚C, 5% CO2 for 48 hours. For RSV plaque assays, overlay containing DMEM, 5% FBS and 0.6% Avicel was applied and plates were incubated at 37˚C, 5% CO2 for 4-5 days. Plates were then fixed with 4% formaldehyde in phosphate buffered solution (PBS) and stained with 0.1% Coomassie Brilliant Blue. Plaques were counted and titre determined as plaque forming units per ml (pfu/ml). Experiments were carried out in technical (n=3) and biological triplicate (n=3 independent experiments). No assumptions about data distribution were made and statistical significance was determined by Mann Whitney U test.

Immunofluorescence and confocal microscopy

Cells were seeded at $2x10^5$ cells/ml on 13 mm glass coverslips or 35mm glass bottom dishes (MATTEK Corporation Inc, USA) prior to infection. Infections were incubated for 24 hours prior to fixation with 4% fomaldehyde in PBS. Fixed cells were permeabilized with 0.1% triton X100 for 10 minutes at room temperature. Samples were blocked with 1% bovine serum albumin (BSA) in PBS for 30 minutes. Primary and secondary antibodies were diluted in 1% BSA in PBS and incubated for 60 minutes at room temperature, followed by four washes with PBS. Coverslips were mounted with Prolong Gold mounting media with DAPI (Invitrogen, USA, P36392), and samples in dishes were stained with 2 µg/ml Hoescht 33342 solution for 10 minutes. For combining mouse primary antibodies, samples were blocked in rabbit serum (Gentex, USA, GTX73221), then stained with primary antibody and rabbit anti-mouse secondary antibody, followed by secondary blocking in donkey serum (Gentex, USA, GTX73205), then stained with primary antibody and donkey anti-mouse secondary antibody. For live-cell imaging, cells were incubated with 2 µg/ml Hoescht 33342 solution in cell

culture media, for 30 minutes at 37˚c. Cells were then washed with cold PBS, followed by incubation with primary antibody diluted in 2% BSA in PBS for 5 minutes on ice. Cells were washed three times with cold PBS and incubated with secondary antibody diluted in 2% BSA in PBS for 5 minutes on ice. Cells were stored in PBS and imaged immediately following staining.

Confocal microscopy was carried out using Zeiss LSM880 AxioObserver microscope (ZEISS, Germany). Standard images were collected using GaAsP detector with 405nm, 488nm and 598nm excitation lasers, using 40x/1.4 or 63x/1.4 plan-apochromat oil DIC M27 objectives. Super-resolution imaging was collected using the Airyscan detector with 405nm, 488nm and 594nm excitation lasers, using plan-apochromat 63x/1.4 oil DIC M27 objective. Z-stacks were collected using a z-interval of 100nm. For determining proportions of infection, fields of view were imaged using 3x3 tile scans at 40x/1.4 oil DIC M27 objective. Image processing and analysis was carried out in ImageJ software (v2.0.0-rc-56/1.52g) (NIH, USA) and Zeiss Zen lite (Blue edition) version 2.6. Single or coinfected cells were counted manually, using cell counter plugin on ImageJ. Experiments were carried out in technical (n=3) and biological triplicate (n=3 independent experiments).

Scanning electron microscopy

Cells were seeded at $2x10^5$ cells/ml on 13 mm glass coverslips prior to infection at MOI of 4 with IAV, RSV or coinfection for 24 hours. Cells were fixed with 1.5% Glutaraldehyde in 0.1M Sodium Cacodylate (SC) buffer for 1 hour and washed 3 times for 5 minutes each with 0.1M SC buffer before incubation with 1% osmium tetroxide for 1 hour. Samples were then stained with aqueous 0.5% Uranyl Acetate for 1 h and further dehydrated through an ethanol series and subjected to critical point drying using an Autosamdri-815 Critical Point Dryer (Tousimis, USA) before mounting and coating in 20nm Gold/Palladium using a Quorum Q150T ES High vacuum coating system (Quorum Technologies, UK). Images were collected using JEOL IT100 SEM at 20kV, with InTouch Scope software, version 1.05 (JEOL USA Inc., USA). Infections and imaging were carried out in two independent experiments, with duplicate samples per experiment.

Cryo-electron Tomography and computational analysis

Cells were seeded at $2x10^4$ cells/ml on laminin-coated gold 200 mesh TEM grids with holey carbon support film (Quantifoil micro tools GmbH, Germany) in 35 mm glass bottom dishes (MATTEK Corporation Inc, USA). Cells were infected with IAV MOI 1 and RSV MOI 4

and incubated for 24 hours at 37˚C. Infections and imaging were carried out in two independent experiments, with duplicate grids images per experiment. For imaging, 5 µl of 15 nm colloidal gold (British Biocell International, UK) was added at a ratio of 1:10 v/v. Grids were then backside blotted for 7 s and plunge frozen into ethane using the Leica EM GP 2 (Leica Microsystems, Germany). Tilt series were acquired using the JEOL CRYO ARM 300 (JEOL Ltd, Japan) equipped with an energy filter and DE64 detector (Direct Electron, USA) with the following parameters: voltage 300 KV, energy filter 30eV slit, 1.921 Å/pixel pixelsize, 30000x magnification, -6 µm defocus, -60˚ to +60˚ tilt with a 3˚ increment, total dose of ~92 e/ Å2 per tilt series. Tilt series were collected using a dose symmetric scheme starting at 0˚ implemented in SerialEM (48). Tilt series were aligned using the alignframes module in IMOD (49). Tomograms were then reconstructed, ctf-corrected using CTFFIND (50) and visualised by weighted back projection using IMOD. To aid interpretation and visualisation, tomograms were binned by a factor of four and then denoised using Topaz (51). Figures and supplemental videos were prepared using IMOD and Quicktime.

Glycoprotein-distance was measured and calculated using the imodinfo module in IMOD. Denoised tomograms were averaged between 5-10 slices to improve contrast and glycoproteins were viewed from top down. Distances were measured between the centres of pairs of adjacent glycoproteins. For IAV and RSV controls, spike measurements were collected from 11 individual tomograms for each virus (n=326 for IAV, n=236 for IAV). For pseudotyped virus, spike measurements were collected from each particle, from 4 individual tomograms (n=50 measurements per tomogram). Normal distribution was tested using Shapiro-Wilk test and statistical difference between groups was determined by unpaired t-test.

Neuraminidase assay

To prepare fresh virus stocks for the neuraminidase assay, A549 cells were seeded at 1x105 cells/well in 24-well plates prior to infection with IAV (MOI of 1), RSV (MOI of 4) or mixed infection. Infected cells were incubated for 24 hours before released virus was harvested from supernatant and cell associated virus was collected by scraping and vortexing infected cells. For the neuraminidase assay, cells were seeded at 1x104 cells/well in 96-well plates, prior to treatment with 1mU/µl neuraminidase from clostridium perfringens (Sigma-Aldrich, USA, N2876) for 2 hours. To confirm removal of sialic acids, neuraminidase treated and control cells were stained with biotinylated Maackia Amurensis Lectin II (MAL II) (Vector

Laboratories, UK, B-1265-1), followed by fluorescein conjugated streptavidin (Vector Laboratories, UK, SA-5001-1) or Erythrina Cristagalli Lectin conjugated to fluorescein (Vector Laboratories, UK, FL-1141-5). Fresh virus stocks were transferred directly onto neuraminidase treated or untreated cells and incubated for 12 hours. Cells were fixed and stained for IAV or RSV nucleoprotein, followed by rabbit anti-mouse 488 (Sigma Aldrich, USA, SABA4600056) secondary antibody. Infected cells were counted using Celigo automated cytometer (Nexcelom Bioscience, USA), using two target expression analysis. Experiments were carried out in biological triplicate (n=3 independent experiments). Variance between groups was not assumed to be equal and statistical difference between conditions was determined by Welch's t-test.

Statistical analysis and Data Visualization

Statistical tests were carried out using Graphpad Prism, version 9.1.0. Data was visualised with RStudio version 1.3.1056 (52) using GGPlot2 package (53).

Methods References

47. C. T. Benfield, J. W. Lyall, G. Kochs, L. S. Tiley, Asparagine 631 variants of the chicken Mx protein do not inhibit influenza virus replication in primary chicken embryo fibroblasts or in vitro surrogate assays. J Virol 82, 7533-7539 (2008).
48. D. N. Mastronarde, Automated electron microscope tomography using robust prediction of specimen movements. J Struct Biol 152, 36-51 (2005).
49. J. R. Kremer, D. N. Mastronarde, J. R. McIntosh, Computer visualization of three-dimensional image data using IMOD. J Struct Biol 116, 71-76 (1996).
50. A. Rohou, N. Grigorieff, CTFFIND4: Fast and accurate defocus estimation from electron micrographs. J Struct Biol 192, 216-221 (2015).
51. T. Bepler, K. Kelley, A. J. Noble, B. Berger, Topaz-Denoise: general deep denoising models for cryoEM and cryoET. Nat Commun 11, 5208 (2020).
52. R. C. Team, R: A language and environment for statistical computing. (2013).
53. Wickham H (2016). ggplot2: Elegant Graphics for Data Analysis. Springer-Verlag New York. ISBN 978-3-319-24277-4, https://ggplot2.tidyverse.org

Extended Data

Contains:

Extended data figures 1-4.
Extended data file 1.
Extended data movie legends 1 and 2.

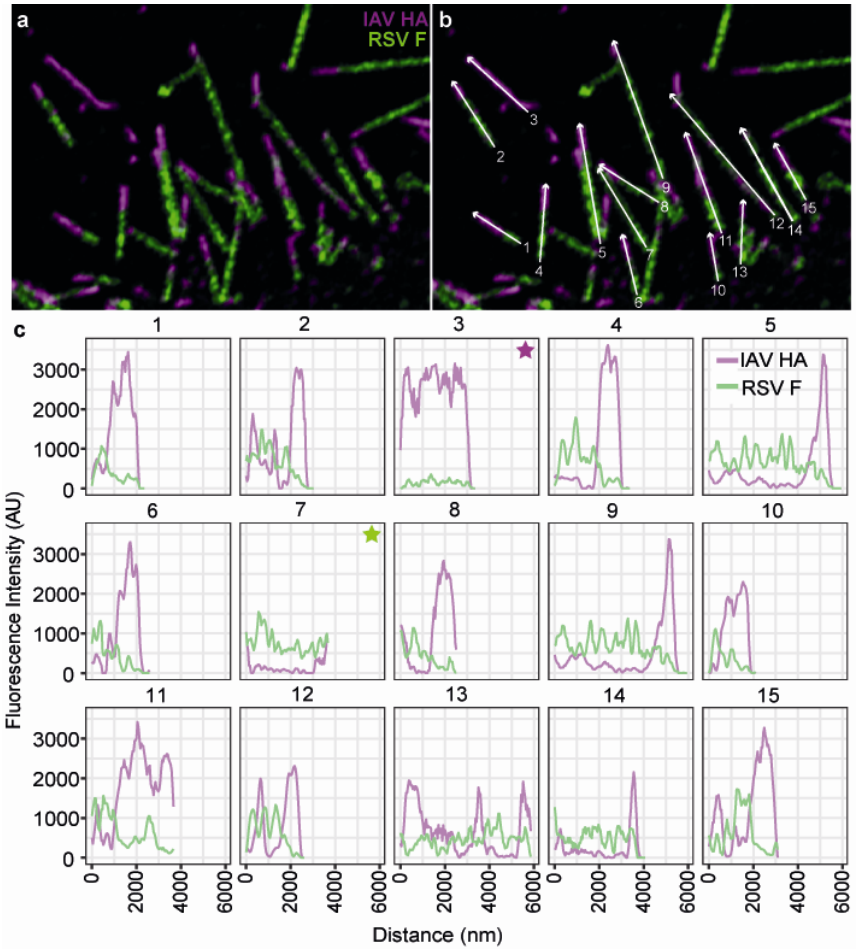

Extended Data Figure 1. HA and F are expressed in discrete patches along the length of filaments, with HA predominantly at the distal end. (**A**) Magnified view of cell associated filaments (full image shown in figure 2A) show filaments with distinct patches of IAV HA (magenta) and RSV F (green) glycoproteins along the length of the filaments. (**B**) White arrows and filament numbering correspond to fluorescence intensity profiles displayed in (**C**). Minimal colocalisation was observed in the fluorescence intensity profiles (**C**) for IAV HA (magenta line) and RSV F (green line) signal along filaments numbered 1-15. IAV (filament 3, magenta star) and RSV (filament 7, green star) filaments were also identified among dual positive filaments.

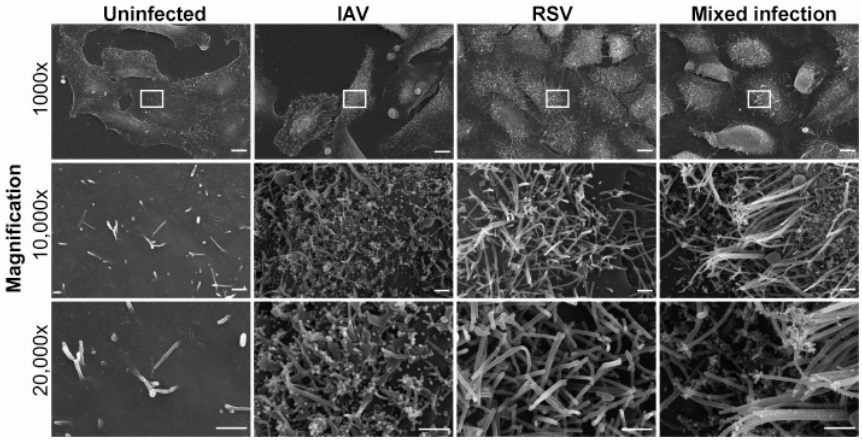

Extended Data Figure 2. Scanning electron microscopy shows clear differences between IAV and RSV virion structure. Scanning electron micrographs of IAV, RSV, coinfected or mock infected cells imaged at 1000x (top row), 10,000x (middle row) and 20,000x (bottom row), region of magnification is denoted by the white box. Scale bars represent 10 µm at 1000x and 1 µm at 10,000x and 20,000x magnification.

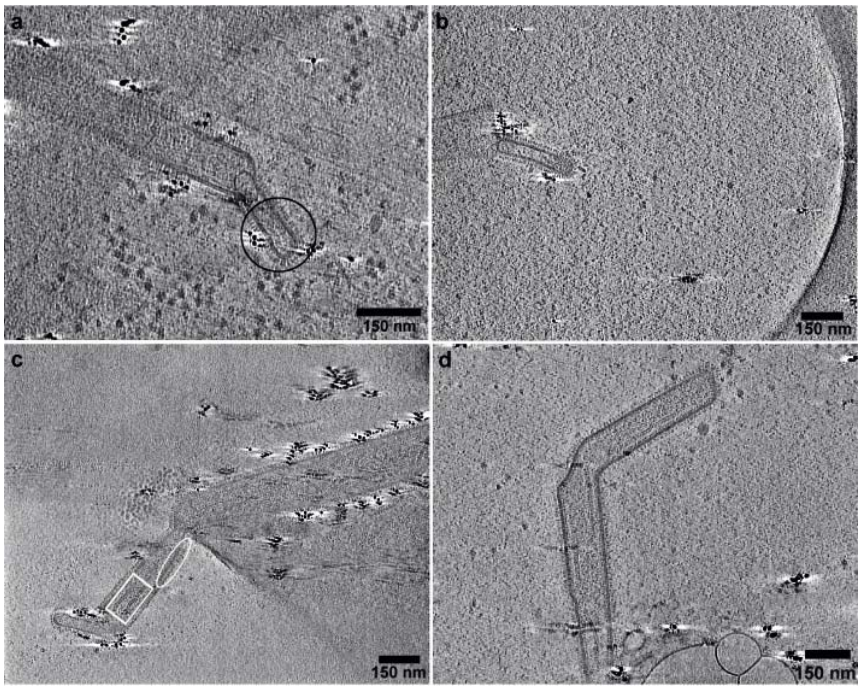

Extended Data Figure 3. Cryo-ET confirmed the presence of chimeric viral particles generated upon co-infection of IAV and RSV. (**A** and **B**) True chimeric virions (CV) displaying both IAV- and RSV-like structural regions joined by a continuous membrane, containing IAV genomes (indicated by black circle in [A]). (**C** and **D**) Pseudotyped virus (PV) that encompassed RSV genomes (indicated by white rectangle in [C]) but were decorated largely with IAV glycoproteins along the viral membrane (indicated by white rectangle in [C]).

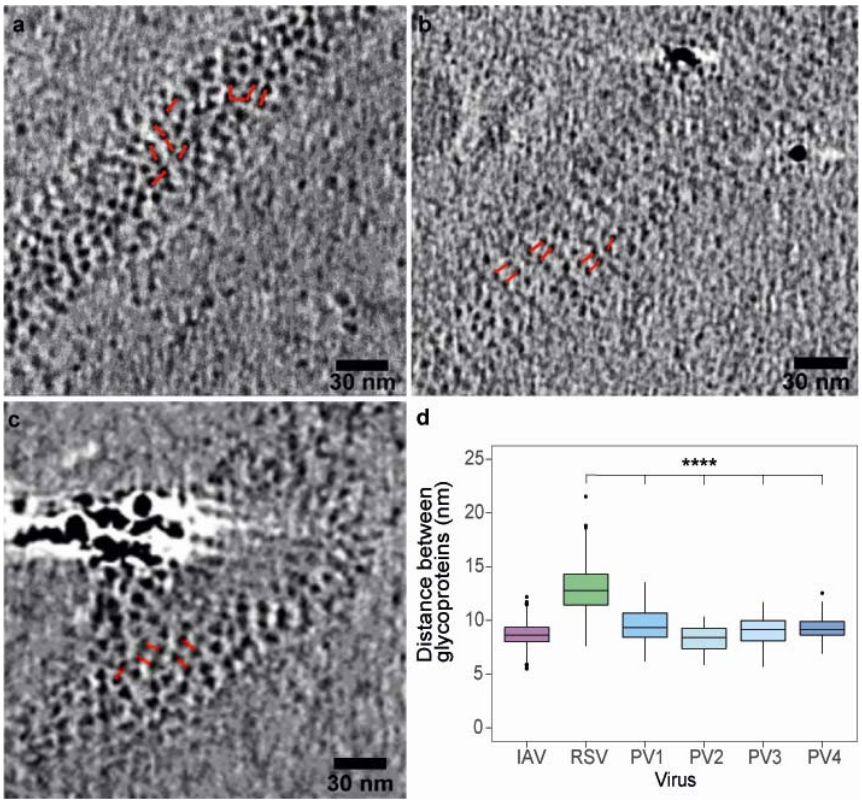

Extended Data Figure 4. Inter-spike distance measurements reveal that pseudotyped viruses are decorated with IAV glycoproteins. To determine the glycoprotein arrangement on pseudotype viruses (PV), inter-spike distances (red lines) were measured between glycoprotein pairs. Representative examples are shown for IAV (**A**), RSV (**B**) and pseudotyped virions (**C**), with red lines demonstrating measurements. Control measurements were collected from 11 tomograms for IAV (measurements n=326) and 11 tomograms for RSV (measurements n=236). PV measurements were collected from 4 individual tomograms (n=50 measurements per tomogram). (**D**) Unpaired t-test analysis confirmed glycoproteins distance measurements were significant different between RSV and PV virions, with average inter-spike distances of 8.71 nm for IAV, 12.9 nm for RSV and a range of 8.31-9.56 nm for PVs.

Extended Data File

Description of IAV and RSV particles

We identified structures consistent with IAV filaments and pleiomorphic particles that were densely coated with glycoproteins (Fig. 1A, Video S1). IAV filaments varied in length, with an average diameter of 84.8 (+/-6.97) nm. IAV ribonucleoproteins (RNPs) could be observed within pleomorphic virions (Figure 1A, Supplementary Video S1). We also identified RSV filaments (Figure 1B, Supplementary video S2) with an average width of 158 (+/-14.6) nm, but many irregular shaped virions were also observed (Fig. 2). Differences in glycoprotein distribution as well as RNP structure between RSV and IAV virions were evident. The glycoproteins in RSV virions exhibited sparser distribution along the virion than IAV glycoproteins (Figs. 1C and 1D). RNPs could be clearly seen in many IAV and RSV filaments. While IAV comprised a single ordered set of RNPs in a "7+1" arrangement at the distal end of filaments, multiple RNPs were detected within RSV filaments having herringbone morphology and ring-like structures attributed to be nucleocapsid (N) or N-RNA assemblies (1, 2) (Fig. 1A-D, Fig. 2). Upon closer inspection of glycoproteins on the surface of virions (top and bottom slices in the tomograms), distinct patterns of glycoprotein arrangement were observed between the two viruses. In IAV virions, glycoproteins were densely packed, devoid of any long-range order, with the "triangular-shaped" trimeric head of HA clearly visible (Fig. 1E, 1F, Fig. 3). However, RSV exhibited a more symmetrical helical arrangement of glycoproteins (striped layers of density) with specific clustering in pairs (Fig. 1G, 1H, Fig. 3), consistent with recent structural studies on RSV filaments (3).

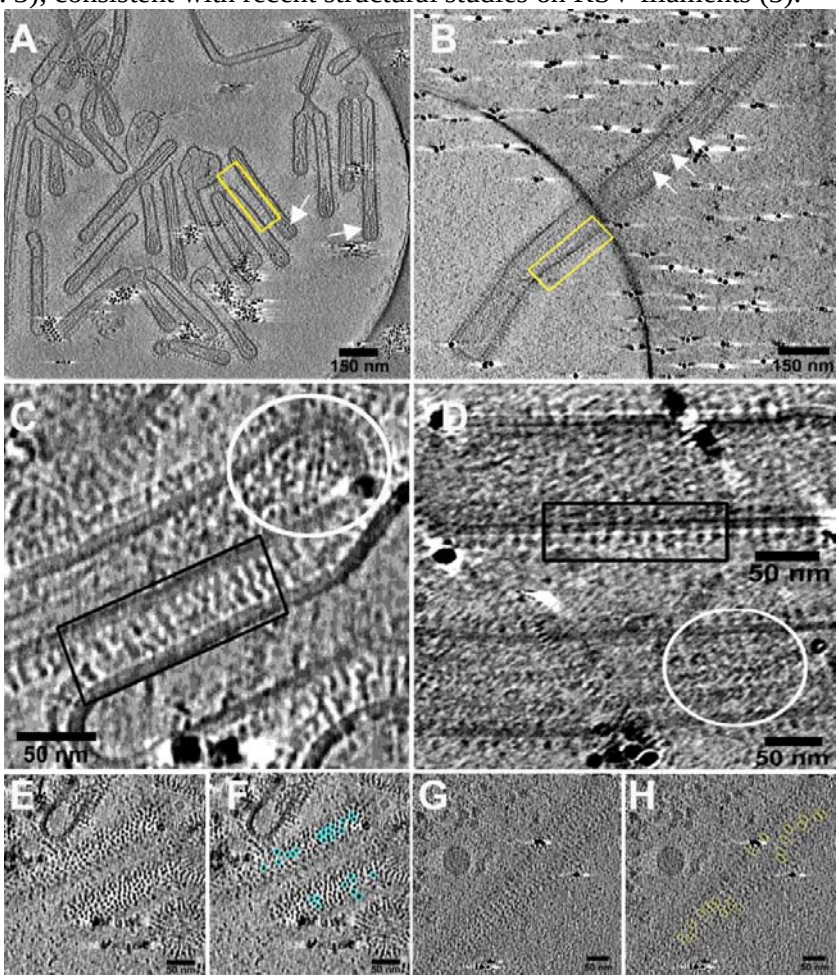

Fig. 1. Cryo-ET shows differences in glycoprotein ordering and RNP organisation between IAV and RSV virions. Cryo-electron tomograms of IAV (**A**) and RSV **(B)** denote pleomorphic morphology alongside differences in glycoprotein and RNP organisation (yellow rectangle and white arrows). IAV virions exhibit a single set of ordered RNPs (**C**, white circle) while multi genomes can be seen in RSV virions (**D**, white circle). Glycoproteins can be seen in a picket fence like distribution along the viral membrane, although more densely packed in IAV than RSV (**C** and **D**, black rectangles). Looking at the glycoproteins from the top and bottom of the virions, significant differences are visible in glycoprotein packing: the triangular hemagglutinin HA spikes on IAV are densely packed with no long-range order (**E** and **F**, cyan circles) while RSV shows clustering of glycoprotein pairs (**G** and **H**, yellow ellipses).

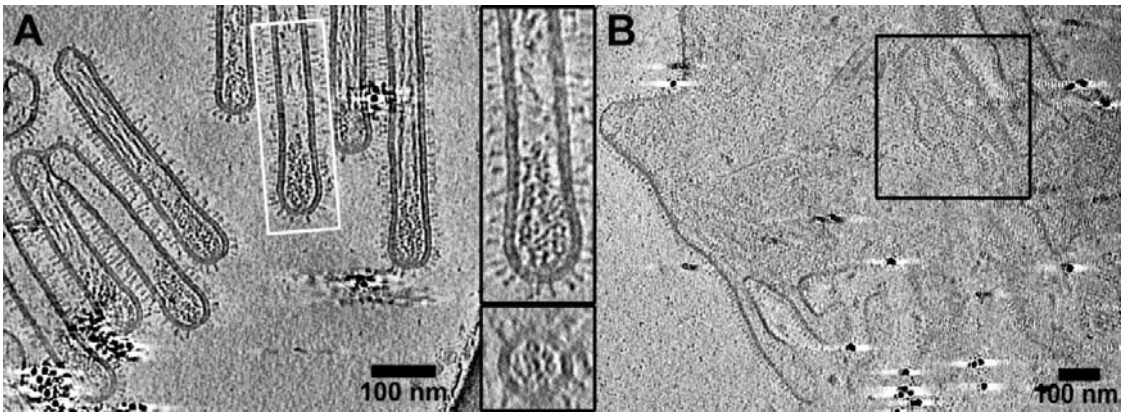

Figure 2. **Distinct RNP organization in IAV and RSV virions seen by Cryo-ET.** (**A**) IAV shows a single ordered set of RNP's at the distal end (white rectangle and magnified view of the same) of filaments. Transverse section (bottom image, magnified view of the white rectangle) of the filament denotes the "7+1" arrangement of RNPs in IAV virions. (**B**) Although RSV can form irregular shaped virions in addition to filaments, they are filled with multiple RNPs inside and decorated with spikes on the outside.

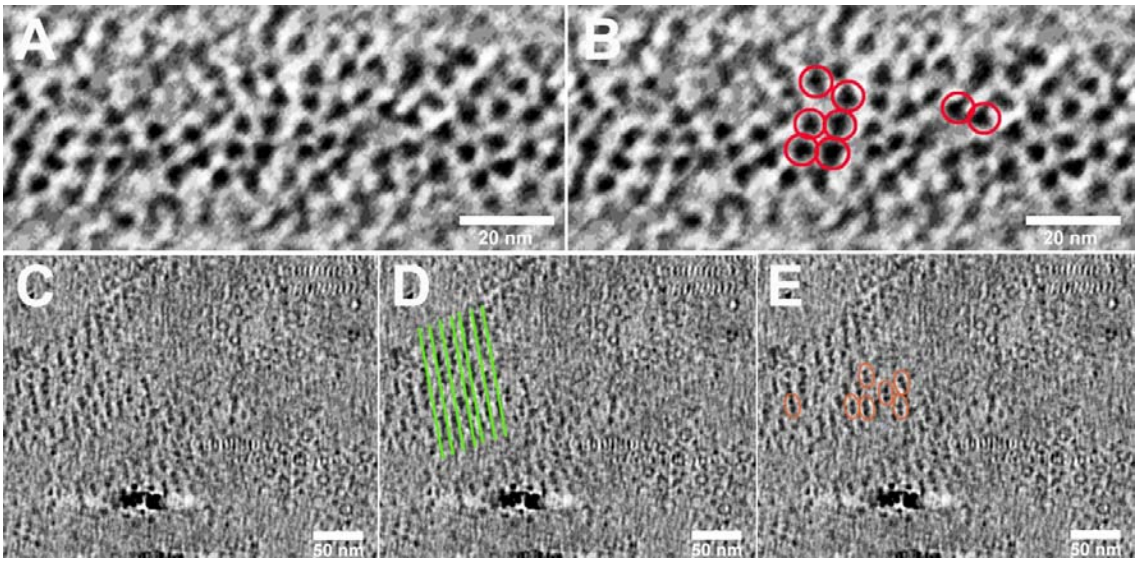

Figure 3. **Different glycoprotein ordering between IAV and RSV virions.**

Inspection of top and bottom views of glycoprotein spikes (corresponding to top and bottom slices of the tomograms) on IAV and RSV virions indicates a different pattern of organization. (**A** and **B**) While the triangular heads (red circles) of the HA glycoprotein in IAV is clearly visible, the spikes are densely packed and devoid of any long-range order. (**C-E**) On the other hand the spikes on RSV appear to be helically ordered as seen by the striped arrays of density (**D**) and specific (**E**) clustering of glycoproteins in pairs (red ellipses) is clearly evident.

Extended Data Movie 1. Video showing serial sections through the z-axis of a tomogram of IAV virions exhibiting pleomorphic morphology. Glycoproteins and RNPs are labelled and denoted by arrows.

Extended Data Movie 2. Video showing serial sections through the z-axis of a tomogram of an RSV filament. Glycoproteins and RNPs are labelled and denoted by arrows.

References

1. L. J. Calder, S. Wasilewski, J. A. Berriman, P. B. Rosenthal, Structural organization of a filamentous influenza A virus. *Proc Natl Acad Sci U S A* **107**, 10685-10690 (2010).

2. D. Bhella, A. Ralph, L. B. Murphy, R. P. Yeo, Significant differences in nucleocapsid morphology within the Paramyxoviridae. *J Gen Virol* **83**, 1831-1839 (2002).

3. M. J. Conley, J. M. Short, J. Hutchings, A. M. Burns, J. Streetley, S. E. Bakker, H. Jaffery, M. Stewart, B. J. Power, G. Zanetti, R. Fearns, S. Vijayakrishnan, D. Bhella, Helical Ordering of Envelope Associated Proteins and Glycoproteins in Respiratory Syncytial Virus Filamentous Virions. *bioRxiv*, 2021.2008.2004.455049 (2021).